Extension of Spatial Filtering Technique Using Kalman Filters for Real-time Pipe Flow Profile Measurements

Jonas Otto[1,*], Tino Steinmetz[1], Martin Schaeper[1], Nils Damaschke[1]

1: Optoelectronics and Photonic Systems, Faculty of Computer Science and Electrical Engineering, University of Rostock, Germany
*Corresponding author: jonas.otto@uni-rostock.de

Keywords: Kalman filter, spatial filtering, velocity measurement, optical measurement technique, noise reduction, pipe-flow profile, real-time flux sensor.

ABSTRACT

Spatial filtering is used for real-time velocity measurement due to its computational efficiency. However, this method can be noisy in real measurement environments, requiring the averaging of a substantial number of measurements to achieve reliable results, which compromises temporal resolution. This study proposes enhancing the spatial filtering algorithm by implementing Kalman filtering for pipe flow profile measurements. Kalman filtering is expected to mitigate the noise issue more effectively than traditional methods like low-pass filtering while maintaining or improving the temporal resolution of measurements.

1. Introduction

Spatial filtering, a technique applied for velocity measurements, is characterized by its real-time processing capability. The spatial filtering technique is used as a process measurement technique for surface velocities (Michel et al. (1998)). Schaeper (2014) has extended the spatial filtering technique to multidimensional velocity measurements in fluid flows. Steinmetz et al. (2023) showed that multidimensional flow fields can be characterized in real-time with a specially developed smart camera using the spatial filtering technique, even at high frame rates. Compared to the PIV or PTV technique, the spatial filtering technique uses selected Fourier coefficients generated via direct weighting with the image data only. Phase jumps in the individual Fourier coefficients generate comparatively high noise components in the spatial filtering signal, necessitating significant data averaging and thus impacting time resolution. Kalman filtering, an algorithmic approach in estimation theory, offers a solution to these challenges. It provides a means to optimally estimate system states in a dynamic and noisy environment, making it a suitable candidate for enhancing spatial filtering algorithms. In this paper, Kalman filters are used to improve the real-time flow measurement of pipe flows.

2. Spatial Filtering Technique

The spatial filtering technique is fundamentally based on employing a periodic, structured grating within the imaging path of an optical system (Aizu & Asakura, 2006; Schaeper et al., 2008). This grating modulates the image information, which is subsequently integrated over time. For a one-dimensional image of a moving structure $i(x - vt)$, the movement translates to a velocity v or a displacement vt in the imaging plane. Utilizing a time-invariant spatial grating function $g(x)$, the spatial filtering signal $s(t)$ can be expressed as (Schaeper & Damaschke, 2012):

$$s(t) = \int_{-\infty}^{\infty} i(x - vt)g(x)\,\mathrm{d}x\,. \tag{1}$$

This signal represents a time-resolved cross-correlation of the imaged structure with the grating function. In this work, complex harmonic grating functions will be used (Schaeper & Damaschke, 2017):

$$g(x) = e^{-\mathrm{j}k_g x}\,, \tag{2}$$

which, when applied to Eq. 1, yields a complex-valued spatial filtering signal:

$$s(t) = \int_{-\infty}^{\infty} i(x - vt)e^{-\mathrm{j}k_g x}\,\mathrm{d}x\,, \tag{3}$$

interpretable as a time-resolved Fourier coefficient of the spatial angular frequency k_g (Schaeper & Damaschke, 2017).

In practical applications, an imaging system with a spatial filter has a finite imaging plane. Assuming the grating function is mean-free and spans an integer multiple N of its period length, Eq. 3 becomes:

$$s(t) = \int_{0}^{NP_n} i(x - vt)e^{-\mathrm{j}k_n x}\,\mathrm{d}x\,. \tag{4}$$

This concept is adaptable to camera systems using CCD or CMOS sensors, where the spatial filtering signal for a region of interest (ROI) can be expressed as:

$$s(t) = \sum_{p=0}^{NP_n-1} i(p - vt)e^{-\mathrm{j}k_n p}\,. \tag{5}$$

Velocity estimation can then be conducted by determining the phase variation in Eq. 1, leveraging the phase difference $\Delta\varphi_g$ of $s(t)$ at discrete time intervals (Nomura et al., 1992):

$$v = \frac{\arg(s(t + \Delta t)) - \arg(s(t))}{k_n \Delta t} = \frac{\arg(s(t + \Delta t)s(t)^*)}{k_n \Delta t} = \frac{\Delta\varphi_g}{k_n \Delta t} \approx \frac{1}{k_n}\frac{\mathrm{d}\varphi}{\mathrm{d}t}\,. \tag{6}$$

Due to finite ROIs, image information crossing boundaries causes spectral inconsistencies, leading to estimation errors. These errors, dependent on image density and ROI shape, necessitate further plausibility checks in processing.

2.1. Temporal Integration

Averaging temporally consecutive values enhances velocity estimation accuracy but reduces temporal resolution. Two methods are viable: computing the average of N_v consecutive velocity estimations:

$$\overline{v} = \frac{1}{N_v} \sum_{i=0}^{N_v-1} v(t_0 + i\Delta t).$$ (7)

This is suitable for dense image information but not for sparse data, where background noise dominates. Alternatively, temporal integration can be performed by accumulating N consecutive complex pointers:

$$I_{\sum}(k) = \sum_{i=0}^{N-1} \left\{ e^{\mathrm{j}\Delta\varphi(k)} |I(k)|^2 \right\}\big|_{t_0+i\Delta t}.$$ (8)

This method is effective for valid signals with equal phases but less advantageous for dense data where errors arise from information changes rather than noise.

2.2. Mean Image Subtraction

To mitigate background illumination effects, subtracting a mean image from the digital data before applying the grating function is effective (Schaeper et al., 2016). The mean image, created by averaging pixel values over several frames, along with a constant threshold, addresses lighting fluctuations and noise. The subtraction results are clipped to zero to prevent negative offsets. The choice between using a mean image or threshold depends on the structure being imaged.

2.3. Multiple Grating Functions

Using a single grating function for spatial filtering, as described by Eq. 1, has limitations. The suitability of the grating function is highly dependent on the spectral content of the imaged structure and its velocity (Schaeper & Damaschke, 2017). A mismatch between the frequency of the grating function and the image's spectral content can render the spatial filtering signal non-evaluable. For example, the correlation with the grating will be zero if the imaged structure is a cosine function with a spatial angular frequency $k_c \neq k_g$.

Multiple grating functions should be used concurrently to mitigate this, generating a set of spatial filtering signals. Evaluating these signals and combining their results can optimize velocity estimation, forming an adaptive spatial filtering algorithm.

A straightforward approach is to apply N different grating functions to the same image and average the resulting independent velocity estimates:

$$\bar{v} = \frac{1}{N} \sum_{n=0}^{N-1} v_n \, . \tag{9}$$

This enhances accuracy but not the dynamic range. When the spatial shift exceeds the smallest period length in the grating set, the estimation quality deteriorates due to phase wrap-around. To address this, we use the approach proposed by Steinmetz et al. (2023), which unwraps phase differences from smaller gratings with respect to larger ones. Using the phase shift $\Delta\varphi_{N-1}$ from the largest grating, an approximation for smaller gratings can be calculated:

$$\Delta\widetilde{\varphi}_n = \frac{P_{N-1}}{P_n} \Delta\varphi_{N-1} \, , \tag{10}$$

Under ideal conditions, this approximation equals the true phase difference $\Delta\varphi_n$ plus an integer multiple M_n of 2π:

$$\Delta\widetilde{\varphi}_n - \Delta\varphi_n = 2\pi M_n \, . \tag{11}$$

M_n can be computed as:

$$M_n = \mathrm{sgn}(\Delta\widetilde{\varphi}_n - \Delta\varphi_n) \left\lceil \frac{|\Delta\widetilde{\varphi}_n - \Delta\varphi_n|}{2\pi} - 0.5 \right\rceil \, . \tag{12}$$

The offset velocity $\widetilde{v}_n$ can then be calculated:

$$v = \frac{1}{N} \sum_{n=0}^{N-1} (v_n + \widetilde{v}_n) \quad \text{where} \quad \widetilde{v}_n = \frac{M_n P_n}{\Delta t} \, , \tag{13}$$

eliminating phase range limitations. However, the maximum estimable velocity remains constrained by the largest grating's period length.

Since we know that the estimation variance is smaller for smaller gratings, a more informed approach to evaluate the estimates generated by the individual gratings then the one in Eq 9, is to form a weighted average with the spatial frequency k_n of each estimation as its weight:

$$\hat{v} = \frac{\sum_{n=0}^{N-1} k_n v_n}{\sum_{n=0}^{N-1} k_n} \, . \tag{14}$$

Alternatively, rearranging Eq. 6 as a linear function of spatial frequency using corrected phase shifts from Eq. 10 allows velocity calculation via linear regression:

$$\Delta\widetilde{\varphi}_n = v\Delta t k_n \, . \tag{15}$$

Which leads to the sum of squared errors objective function:

$$\text{SSE} = \sum_{n=0}^{N} (\Delta\widetilde{\varphi}_n - v\Delta tk_n). \tag{16}$$

After setting the derivative to zero and solving for v, we get:

$$\hat{v} = \frac{\sum_{n=0}^{N} \Delta tk_n \Delta\widetilde{\varphi}_n}{\sum_{n=0}^{N} (\Delta tk_n)^2}. \tag{17}$$

3. Kalman Filter

We employ a Kalman filter first introduced by Kalman (1960) to enhance the accuracy and temporal resolution of velocity measurements in spatial filtering. This methodology allows us to effectively manage the inherent noise in spatial filtering while maintaining real-time processing capabilities. By continuously updating the estimates based on new measurements, the Kalman filter dynamically adapts to changes in the velocity field, offering a significant improvement over static averaging methods.

The Kalman filter is a recursive algorithm that efficiently processes noisy measurements to produce estimates of unknown variables. At its core, the Kalman filter operates in two primary steps: prediction and update.

3.1. Prediction Step

In the prediction phase, the filter uses a model of the system to forecast the next state, represented as:

$$\hat{\mathbf{x}}_{k|k-1} = \mathbf{F}_k \hat{\mathbf{x}}_{k-1|k-1} + \mathbf{B}_k \mathbf{u}_k, \tag{18}$$

where $\hat{\mathbf{x}}_{k|k-1}$ is the predicted state, $\mathbf{F}_k$ the state transition model, $\hat{\mathbf{x}}_{k-1|k-1}$ the previous estimated state, $\mathbf{B}_k$ the control-input model, and $\mathbf{u}_k$ the control vector. In our specific application, $\mathbf{B}_k$ and $\mathbf{u}_k$ are not applicable, which simplifies Eq. 18 to:

$$\hat{\mathbf{x}}_{k|k-1} = \mathbf{F}_k \hat{\mathbf{x}}_{k-1|k-1}. \tag{19}$$

The predicted state covariance matrix $\mathbf{P}_{k|k-1}$ is given by:

$$\mathbf{P}_{k|k-1} = \mathbf{F}_k \mathbf{P}_{k-1|k-1} \mathbf{F}_k^T + \mathbf{Q}_k, \tag{20}$$

where $\mathbf{Q}_k$ is the process noise covariance matrix.

3.2. Update Step

In the update phase, the filter incorporates the new measurement $\mathbf{z}_k$, adjusting the predicted state using the Kalman gain $\mathbf{K}_k$:

$$\mathbf{K}_k = \mathbf{P}_{k|k-1}\mathbf{H}_k^T(\mathbf{H}_k\mathbf{P}_{k|k-1}\mathbf{H}_k^T + \mathbf{R}_k)^{-1} \tag{21}$$

$$\hat{\mathbf{x}}_{k|k} = \hat{\mathbf{x}}_{k|k-1} + \mathbf{K}_k(\mathbf{z}_k - \mathbf{H}_k\hat{\mathbf{x}}_{k|k-1}) \tag{22}$$

$$\mathbf{P}_{k|k} = (\mathbf{I} - \mathbf{K}_k\mathbf{H}_k)\mathbf{P}_{k|k-1} \tag{23}$$

Here, $\mathbf{P}_{k|k}$ is the updated state covariance, $\mathbf{H}_k$ the observation model, and $\mathbf{R}_k$ the observation noise covariance.

3.3. State Space Representation

The underlying process and the specific application determine the number of state dimensions in the Kalman filter. For a system assuming constant velocity, a two-dimensional state vector $[\mathbf{s}, \mathbf{v}]^T$ suffices. The state transition model $\mathbf{F}_k$ is then represented using the classical equations of motion:

$$\mathbf{F}_k = \begin{pmatrix} 1 & \Delta t \\ 0 & 1 \end{pmatrix} \tag{24}$$

where Δt is the time step between state updates. However, for more dynamic systems where acceleration is significant, a three-dimensional state vector $[\mathbf{s}, \mathbf{v}, \mathbf{a}]^T$ with the state transition model:

$$\mathbf{F}_k = \begin{pmatrix} 1 & \Delta t & \frac{1}{2}\Delta t^2 \\ 0 & 1 & \Delta t \\ 0 & 0 & 1 \end{pmatrix} \tag{25}$$

is necessary. The choice between two and three state dimensions depends on the velocity field's nature and the observed system's dynamics. If the acceleration is negligible, a two-dimensional model is adequate. Conversely, if the system exhibits significant changes in acceleration, a three-dimensional model provides a more accurate representation.

3.4. Process Noise Covariance Matrix Q

The process noise covariance matrix $\mathbf{Q}$ reflects the uncertainty in the model itself, accounting for unmodeled dynamics and external perturbations. For our system, $\mathbf{Q}$ is:

$$\mathbf{Q} = \begin{pmatrix} \sigma_s^2 & 0 & 0 \\ 0 & \sigma_v^2 & 0 \\ 0 & 0 & \sigma_a^2 \end{pmatrix} \tag{26}$$

where σ_s^2, σ_v^2, and σ_a^2 are the variances of the distance, velocity, and acceleration process noise, respectively. These variances can be determined based on the physical characteristics of the system and the expected magnitude of the unmodeled dynamics.

3.5. Measurement Noise Covariance Matrix R

The measurement noise covariance matrix $\mathbf{R}$ characterizes the noise associated with the measurement process. This matrix encapsulates the measurement noise variance, which originates from sensor inaccuracies and other external factors affecting the measurements. Denoting the measurement noise variances for the distance, velocity, and acceleration sensors as $\sigma_{z_s}^2$, $\sigma_{z_v}^2$, and $\sigma_{z_a}^2$, respectively, $\mathbf{R}$ is formulated as:

$$\mathbf{R} = \begin{pmatrix} \sigma_{z_s}^2 & 0 & 0 \\ 0 & \sigma_{z_v}^2 & 0 \\ 0 & 0 & \sigma_{z_a}^2 \end{pmatrix} \tag{27}$$

3.6. Integration of the Kalman Filter in Spatial Filtering

The proposed methodology involves integrating Kalman filtering with the existing spatial filtering algorithm to enhance noise reduction capabilities without compromising real-time processing. The adaptability of Kalman filtering parameters allows for fine-tuning to suit the velocity measurement system's specific dynamics and noise characteristics.

When using multiple gratings for spatial filtering, as proposed in Schaeper (2014), the estimation from each grating can be combined via sensor fusion in the Kalman filter. Alternatively, the estimates from each grating can be first evaluated to produce a single value per measurement, which then serves as the only input for the Kalman filter. To account for varying velocities across different regions of an image when measuring flow, a separate Kalman filter is used for each interrogation area, operating in parallel.

4. Simulation

4.1. Methodology

To accurately assess the performance of the Kalman filter in comparison to the unfiltered spatial filter, we evaluate images generated by a simulation with a defined pixel displacement. The images are produced by creating a canvas with a particle concentration of one particle per 100 pixels, with a slight Gaussian blur applied to simulate slightly out-of-focus imaging. Each frame is captured by moving a virtual camera over the canvas by a predetermined shift, resulting in a series of 5000
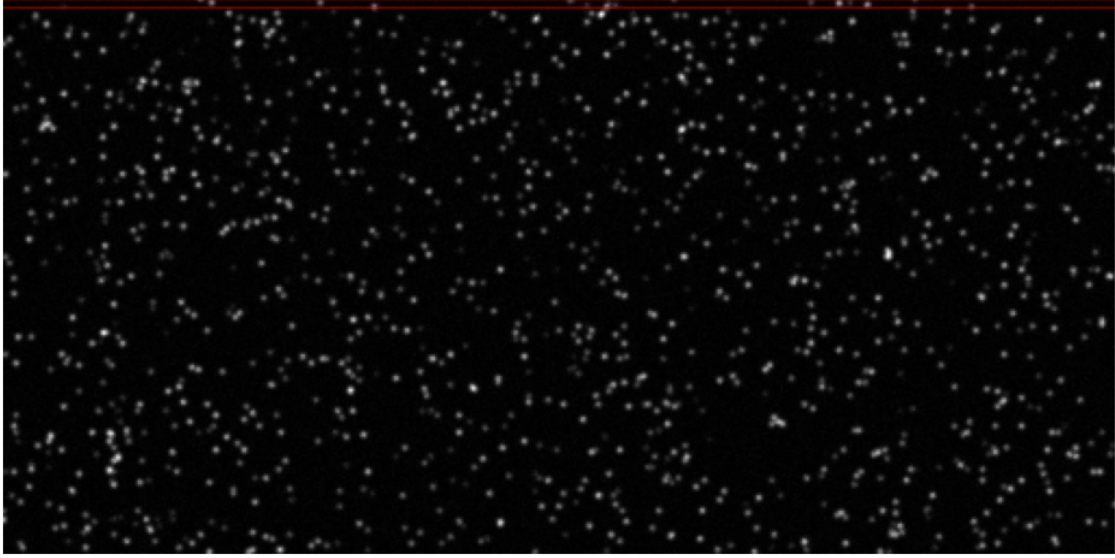
Figure 1. Simulated Image of particles. Selected Interrogation Area marked in red.

images with dimensions of $256\,\mathrm{px} \times 512\,\mathrm{px}$ and a constant pixel shift of $0.2\,\mathrm{px}$ to $20\,\mathrm{px}$. Unlike real-world pipe flow, where different regions move at varying speeds, the uniform velocity across these images limits our evaluation to individual interrogation areas. For this study, we select one interrogation area, consisting of the four uppermost lines as indicated in Fig. 1.

Temporal integration of ten images per measurement is employed. Assuming a sampling rate of $1000\,\mathrm{Hz}$, with an integration time of ten, we obtain a measurement rate of $100\,\mathrm{Hz}$, corresponding to a measurement interval of $\Delta \mathrm{t} = 0.01\,\mathrm{s}$.

The spatial filter utilizes eight gratings with period widths of $12, 14, 16, 20, 24, 32, 48$, and $64\,\mathrm{px}$. To ensure a dynamic range of up to $20\,\mathrm{px}$, the phase of the grids with smaller period widths must be unwrapped according to the algorithm in Section 2.3.

Two distinct approaches are employed for the Kalman filtering. The first approach involves taking the single measurement for each timestep from the spatial filter, evaluated via linear regression, as a single input for the Kalman filter, constituting a one-dimensional Kalman filter. The second approach assumes the measurement values for each grating to be independent sensor outputs. The Kalman filter then incorporates all these inputs to perform sensor fusion, yielding a single measurement for each time step.

Given that we assume constant velocity, we define two state dimensions: position and velocity. The state vector is thus $\mathbf{x} = [s, v]^T$.

The initial state covariance matrix $\boldsymbol{P}$ is set as:

$$\boldsymbol{P} = \begin{bmatrix} 1 & 0 \\ 0 & 1 \end{bmatrix} \tag{28}$$

Given that the simulation ensures a completely constant velocity, the process noise covariance matrix $\boldsymbol{Q}$ is defined as:

$$\boldsymbol{Q} = \begin{bmatrix} \sigma^2 \Delta t & 0 \\ 0 & \sigma^2 \Delta t \end{bmatrix} \tag{29}$$

where $\sigma^2 = 0.1$.

The measurement noise covariance matrix $\boldsymbol{R}$ is parameterized by the variance of each sensor input. For the first approach, it is a scalar value, whereas for the second approach, it is an 8x8 matrix. The matrices are defined as:

$$\boldsymbol{R}_{\text{approach 1}} = \sigma^2_{\text{sensor}} \tag{30}$$

$$\boldsymbol{R}_{\text{approach 2}} = \begin{bmatrix} \sigma_1^2 & 0 & \cdots & 0 \\ 0 & \sigma_2^2 & \cdots & 0 \\ \vdots & \vdots & \ddots & \vdots \\ 0 & 0 & \cdots & \sigma_8^2 \end{bmatrix} \tag{31}$$

4.2. Results

The simulation results illustrate the performance enhancement achieved by integrating Kalman filters with the spatial filtering technique. The primary metric used for comparison is the Root Mean Square Error (RMSE) between the estimated and true displacements across varying pixel displacements.

Figure 2 presents a detailed comparison of the RMSE values for different filtering techniques as a function of displacement. The Kalman filter significantly reduces the estimation error, demonstrating its effectiveness in improving the accuracy of velocity measurements in a noisy environment.

The mean RMSE values for each technique are summarized as follows:

- **Spatial Filter Mean:** $0.1229\,\text{px}$

- **Spatial Filter Weighted Average:** $0.0777\,\text{px}$

- **Spatial Filter Regression:** $0.0680\,\text{px}$

- **Spatial Filter Regression + 1D Kalman Filter:** $0.0174\,\text{px}$

- **Spatial Filter + 2D Kalman Filter:** $0.0183\,\text{px}$

These results indicate that applying the Kalman filter substantially reduces the RMSE, thus enhancing the precision of displacement estimation. The two implementations of the Kalman filter
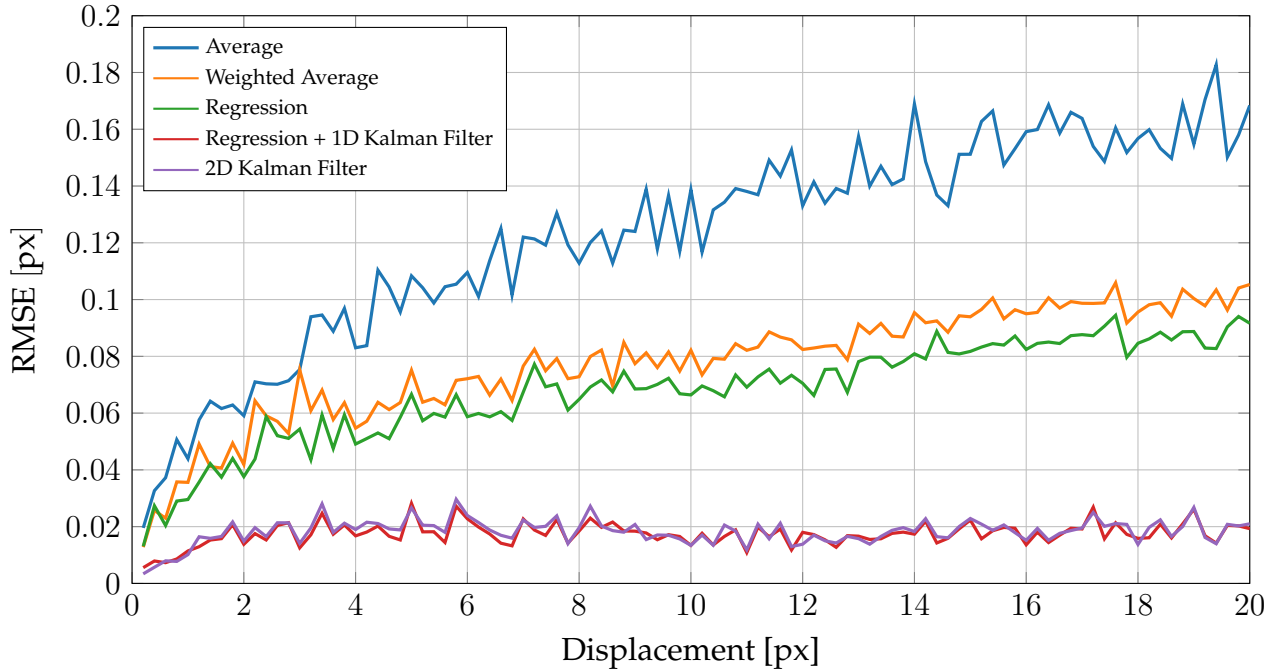
Figure 2. RMSE comparison between different spatial filtering techniques with and without Kalman filtering.

appear to be closely matched; however, in this experiment, the 1D Kalman filter for the spatial filter, evaluated via linear regression, performs the best.

As an example, Fig. 3 further illustrates the effectiveness of the Kalman filter. It shows the displacement estimation over time for a constant true displacement of $10\,\text{px}$. The blue line represents the raw spatial filter estimation, which exhibits significant noise and fluctuation. The orange line, indicating the Kalman filter output, closely follows the true displacement (shown in red), demonstrating the filter's capability to smooth out noise and provide a more accurate estimate.

Integrating the Kalman filter enhances the accuracy and maintains the temporal resolution of the measurements. The Kalman filter's recursive nature allows it to adapt to changes in the velocity field dynamically, providing real-time updates that significantly outperform static averaging methods.

5. Measurement

5.1. Measurement Setup

The real-time measurement system presented in Steinmetz et al. (2023) was used to determine the one-dimensional velocity profile in a pipe with a circular cross-section. For this purpose, a pipe flow through a transparent pipe section was illuminated using a $532\,\text{nm}$ cw laser light sheet. An
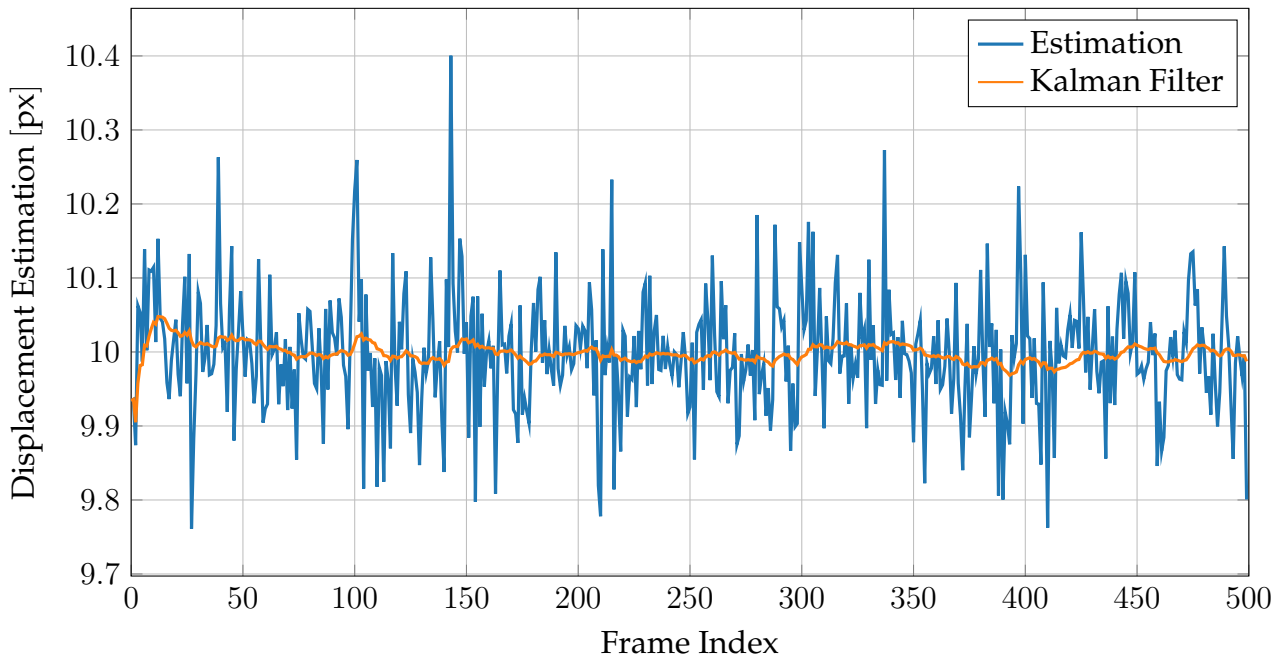
Figure 3. Displacement estimation over time for a simulated displacement of 10 px per image using spatial filtering with and without Kalman filtering.

adjustable pump controls the fluid flow within this tube. The smart camera was placed at a small angle to the light sheet so that sufficient scattered light was available and the entire cross-section of the pipe flow could be observed (Fig. 4). No additional plane windows or liquid prisms were used.
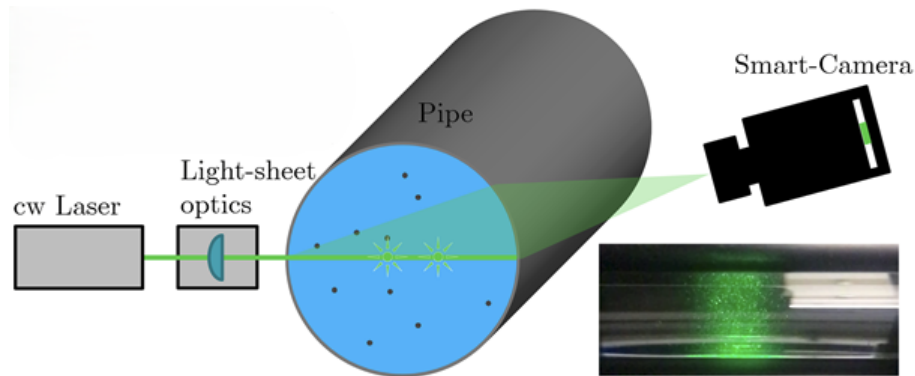

Figure 4. Optical sensor configuration for real-time measurement of pipe flow profiles

Because of the inclined direction of observation and the curvature of the pipe, the image of the measuring section is distorted. In the flow direction, the measured pixel offset scales with the radial coordinate in the pipe. The local resolution and, therefore, the width of the interrogation areas perpendicular to the direction of flow is influenced, on the one hand, by the perspective and, on the other hand, slightly by the curvature of the pipe. This means that the interrogation areas no

longer scan the flow equidistantly regarding radial location. In contrast to calibration in the classic PIV technique, the distortions in the image were not corrected before processing, but the results were weighted by a distortion factor. This has the advantage that the computationally complex velocity determination takes place directly on the original image, and only a few integral pixel offset values need to be corrected. This approach can be used because the flow and image velocity are constant along an interrogation area or in the pipe direction.

Over the pipe diameter of $20\,\text{mm}$, 64 interrogation areas with a size of $4\,\text{px} \times 512\,\text{px}$ were captured in a region of interest of $256\,\text{px} \times 512\,\text{px}$. The images were processed in real time using the FPGA smart camera at a frame rate of $100\,\text{Hz}$ and temporal integration of ten images for four grids, resulting in time-resolved pipe flow profiles.

5.2. Mean flow profile estimation

The left part of Fig. 5 shows the mean flow profiles for different turbulent flow rates without any distortion correction. The frequency of the pump in the legend specifies the flow rate. The higher degrees of turbulence for larger flow rates and the higher standard deviations in the area of velocity gradients can be recognized. The Kalman filter can be directly applied to the uncorrected pixel shifts.
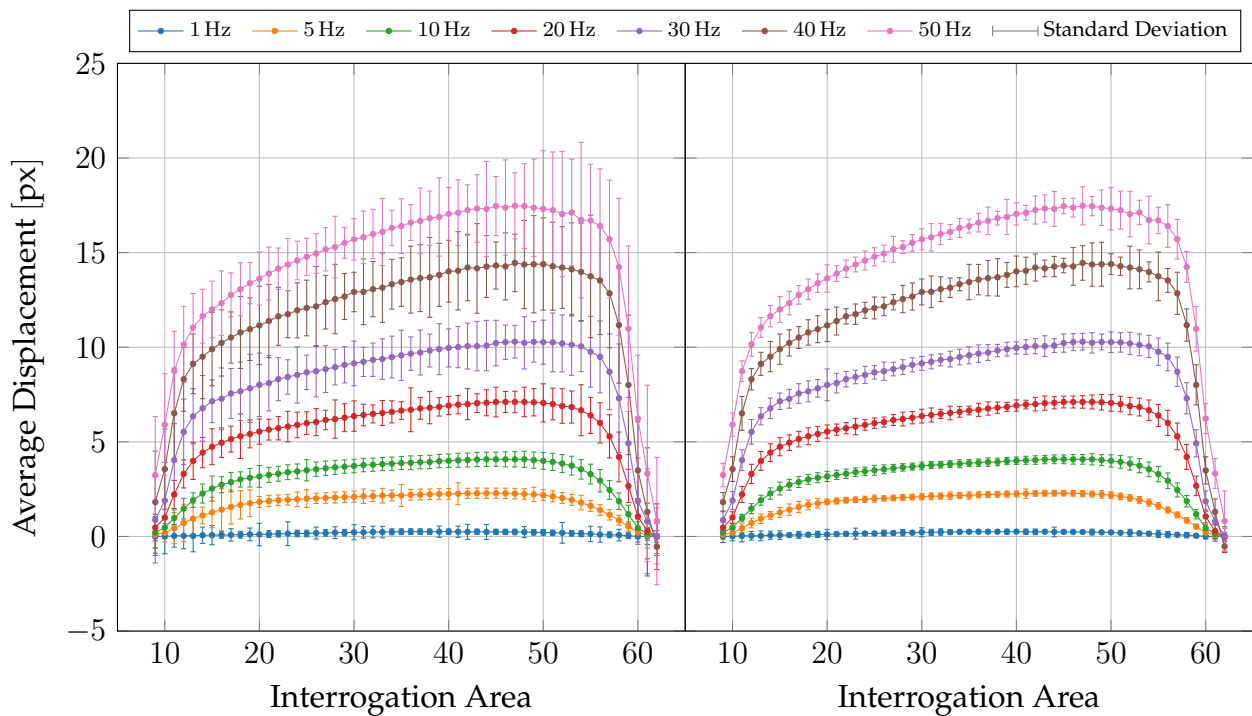

Figure 5. Pipe flow profiles for different pump revolutions per second measured by the smart-camera real-time sensor. Mean values of measurements on the left, mean values of Kalman filtered measurements on the right.

In the left plot of Fig. 5, which represents the results obtained using the conventional spatial filter without Kalman filtering, the standard deviation of the displacement measurements is significantly higher across all frequencies and interrogation areas. This increased variability indicates a higher level of noise and uncertainty in the measurements, particularly in regions of higher displacement.

Conversely, the right plot of Fig. 5, which shows the measurements with the Kalman filtered spatial filter, exhibits substantially reduced standard deviations. The Kalman filter effectively smooths the displacement measurements, resulting in more consistent and reliable data across all interrogation areas. This improvement is especially noticeable at higher frequencies, where the standard deviations in the Kalman-filtered results are markedly lower compared to the non-filtered results.

The Kalman filter reduces variations due to velocity estimation and fluctuations due to turbulence. With the high sampling rates of the system ($1000\,\text{Hz}$), however, it would also be possible to reconstruct the low-frequency part of the turbulence spectrum. This is the subject of current research in combination with the design of the Kalman filter.

These findings underscore the advantage of using the Kalman filter in conjunction with spatial filtering for real-time flow measurements. By significantly reducing the standard deviation, the Kalman filter enhances the accuracy and reliability of the displacement estimates, providing a more robust measurement technique suitable for applications requiring high precision.

5.3. Profile correction

After estimating the pixel offset and applying the Kalman filter, the optical distortion must be corrected to reconstruct the flow profile. Due to the developed turbulent flow profile, the profile is radially symmetrical. The slope of the uncorrected profile is due to the perspective distortion. The profiles were interpolated by a polynomial. It is interesting to note that the even order n of the polynomial increased for higher flow velocity, but only 5 coefficients c_0, c_1, c_2, c_4, c_n and the radial position of the pipe axis r_0 were necessary to fit the pixel offset profile (see Fig. 6 left).

$$\overline{\Delta p}(r) = c_0 + c_1(r - r_0)^1 + c_2(r - r_0)^2 + c_4(r - r_0)^4 + c_n(r - r_0)^n \tag{32}$$

The odd coefficient c_1 represents the perspective-related gradient of the uncorrected profile. In relation to the pixel offset in the centre $c_1 / \overline{\Delta p}(r_0)$ of the flow profiles, this coefficient is almost the same for all radially symmetrical profiles. The distortion of the flow profile can be corrected by setting the coefficient $c_1 = 0$ (see Fig. 6 right).

Figure 7 left shows the corrected profiles with mean value and standard deviation. The pixel offset values and the standard deviations were weighted with the correction factor determined above. The increase in the standard deviation for higher flow velocities can be seen, which corresponds to the expected increase in the turbulence level. Furthermore, larger standard deviations can be
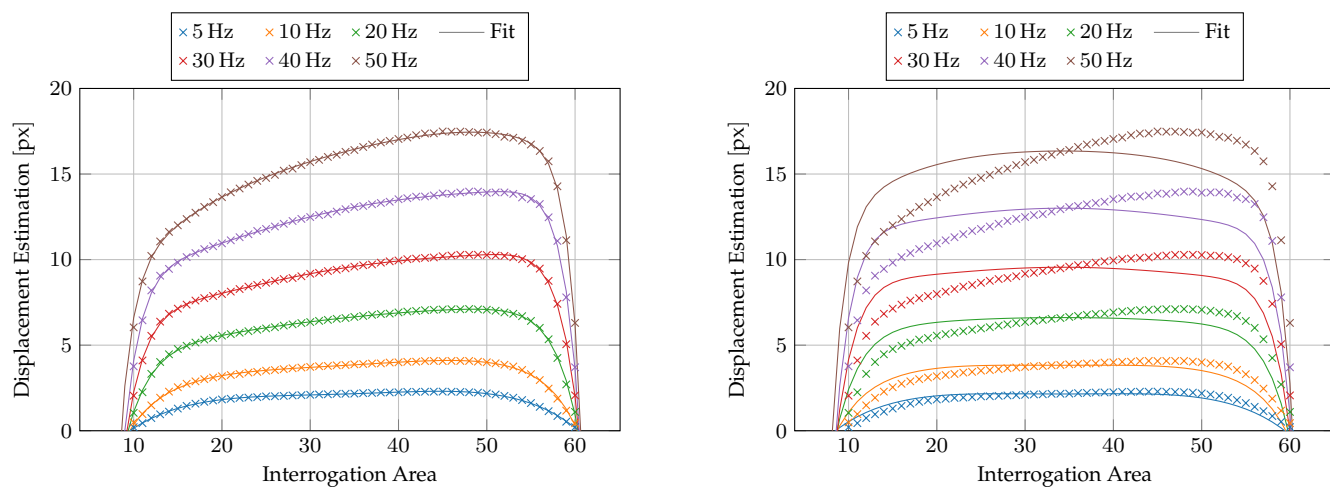
Figure 6. Estimation of the perspective correction of the flow profiles from coefficients of a polynomial fit. Left: Uncorrected profiles and polynomial fit with gradient in the pipe axis. Right: Uncorrected profiles and corrected symmetric polynomial
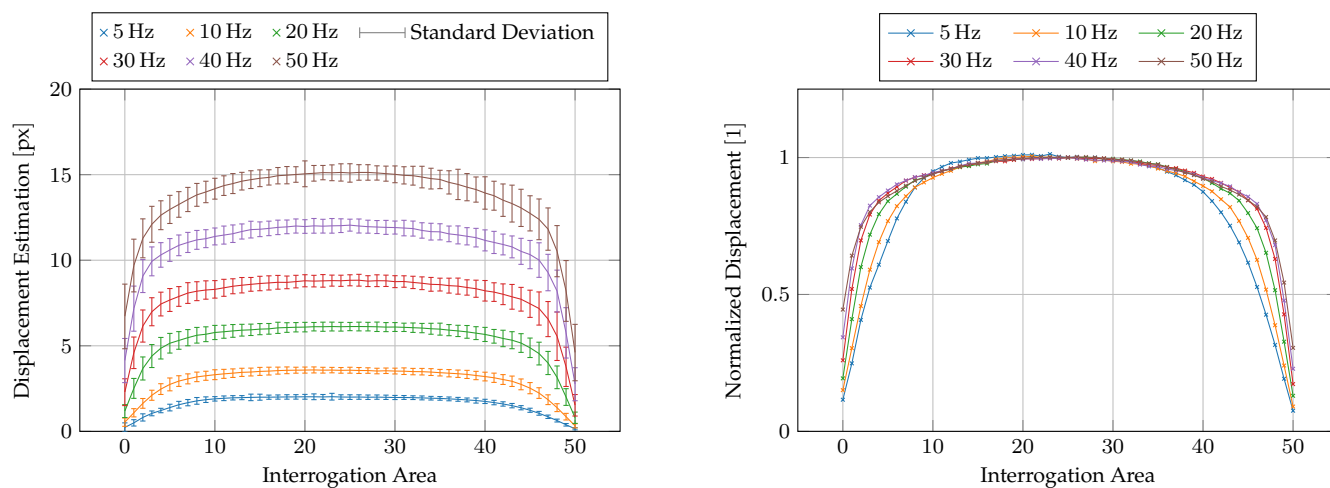

Figure 7. Perspective-corrected flow profiles. Left: Profiles with standard deviation. Right: Profiles normalized to maximum velocity

recognized in the area of large velocity gradients near the walls of the pipe. These are caused by radial averaging over the detection volume of an interrogation area Durst et al. (1998).

Finally, in Fig. 7 right, the flow profiles are normalized to their maximum velocity in the pipe axis. In this representation, the increase in the polynomial order n for increasing velocities is very clearly recognizable. Again, however, only a description with 4 coefficients and the position of the pipe axis r_0 is sufficient

$$\overline{\Delta p}(r) = c_0 + c_2(r - r_0)^2 + c_4(r - r_0)^4 + c_n(r - r_0)^n \tag{33}$$

6. Conclusion

This study presents the integration of Kalman filtering with the spatial filtering technique to enhance the accuracy and temporal resolution of real-time velocity measurements in pipe flow profiles. The simulation and experimental results underscore the effectiveness of this approach. The application of the Kalman filter significantly reduces the RMSE of displacement estimates, thus improving the precision of velocity measurements under noisy conditions. Notably, the Kalman filter maintains the temporal resolution by dynamically updating estimates based on incoming measurements, outperforming traditional static averaging methods.

While the Kalman filter offers substantial improvements in measurement accuracy and reliability, it is essential to recognize the constraints and potential areas for further refinement. The current implementation assumes a relatively constant velocity field, which may not hold in highly dynamic or turbulent flow conditions.

References

Aizu, Y., & Asakura, T. (2006). *Spatial filtering velocimetry: Fundamentals and applications* (Vol. 116). Springer Science & Business Media.

Durst, F., Fischer, M., Jovanovic´, J., & Kikura, H. (1998, 09). Methods to Set Up and Investigate Low Reynolds Number, Fully Developed Turbulent Plane Channel Flows. *Journal of Fluids Engineering*, *120*(3), 496-503. Retrieved from `https://doi.org/10.1115/1.2820690` doi: 10.1115/1.2820690

Kalman, R. E. (1960, 03). A New Approach to Linear Filtering and Prediction Problems. *Journal of Basic Engineering*, *82*(1), 35-45. Retrieved from `https://doi.org/10.1115/1.3662552` doi: 10.1115/1.3662552

Michel, K., Christofori, K., Bergeler, S., Richter, A., Kumpart, J., Krambeer, H., & Fiedler, O. (1998). Miniaturized spatial filtering velocimeter for industrial applications. , *2*, 893-897 vol.2. doi: 10 .1109/IMTC.1998.676853

Nomura, M., Hori, M., Shimomura, J., & Terashima, M. (1992). Velocity measurement using phase orthogonal spatial filters. In *Conference record of the 1992 ieee industry applications society annual meeting* (pp. 1756–1761).

Schaeper, M. (2014). *Mehrdimensionale ortsfiltertechnik* (PhD thesis). Universität Rostock.

Schaeper, M., & Damaschke, N. (2012). Pre-processing for multidimensional spatial filtering technique. In *16th int. symp. on application of laser techniques to fluid mechanics.*

Schaeper, M., & Damaschke, N. (2017). Fourier-based layout for grating function structure in spatial filtering velocimetry. *Measurement Science and Technology*, *28*(5), 055008.

Schaeper, M., Menn, I., Frank, H., & Damaschke, N. (2008). Spatial filtering technique for measurement of 2c flow velocity. In *Proceedings of 14th international symposium on applications of laser techniques to fluid mechanics, 7th-10th july.*

Schaeper, M., Schmidt, R., Kostbade, R., Damaschke, N., & Gimsa, J. (2016). Optical high-resolution analysis of rotational movement: testing circular spatial filter velocimetry (csfv) with rotating biological cells. *Journal of Physics D: Applied Physics*, *49*(26), 265402.

Steinmetz, T., Schaeper, M., Kleinwächter, A., Otto, J., Richter, A., Poosch, R., & Damaschke, N. (2023). Time-resolved determination of velocity fields on the example of a simple water channel flow, using a real-time capable fpga-based camera platform. *Experiments in Fluids*, *64*(4), 73. Retrieved from `https://doi.org/10.1007/s00348-023-03617-8` doi: 10.1007/s00348 -023-03617-8